Materialia 14 (2020) 100902

Contents lists available at ScienceDirect

Materialia

journal homepage: www.elsevier.com/locate/mtla

Full Length Article

Processing 4th generation titanium aluminides via electron beam based additive manufacturing – characterization of microstructure and mechanical properties

M. Reith[a,*], M. Franke[a], M. Schloffer[b], C. Körner[a,c]

[a] Neue Materialien Fürth GmbH, Dr.-Mack-Str. 81, 90762 Fürth, Germany
[b] MTU Aero Engines AG, Dachauer Str. 665, 80995 Munich, Germany
[c] Chair of Materials Science and Engineering for Metals, Friedrich-Alexander University Erlangen-Nürnberg, Martensstr. 5, 91058 Erlangen, Germany

ARTICLE INFO

Keywords:
Titanium aluminides
Additive manufacturing
Mechanical properties
Tensile test
Creep

ABSTRACT

Lightweight intermetallic γ-titanium aluminides (TiAl) based alloys are used for high temperature applications in advanced aerospace and automotive engines. Normally, these alloys are processed via investment casting as well as wrought processing, e.g. hot-forging. The feasibility of processing γ-TiAl via electron beam powder bed fusion (PBF-EB/M) is already demonstrated for various titanium aluminides. Due to the high reactivity of titanium aluminides, electron beam powder bed fusion is a promising manufacturing technique which provides dense components with only small variations in the aluminum (Al) content when using accurately optimized process parameters. However, the processing and machining of γ-TiAl based alloys is challenging due to their high reactivity as well as low ductility and fracture toughness at room temperature (RT). The present paper is focusing on the characterization of a 4th generation γ-TiAl based alloy with the nominal composition Ti–47.5Al–5.5Nb–0.5 W (at.%), customized for additive manufacturing process. The high amount of aluminum ensures a peritectic solidification and improves the room temperature ductility. Niobium and Tungsten provide sufficient high temperature strength and creep resistance. However, the processability of a novel alloy via PBF-EB/M is challenging. Therefore, accurately optimized PBF-EB/M parameters are used for the processing of this 4th generation γ-TiAl powder in order to avoid defects and inhomogeneous microstructures. The subsequent material characterization is based on numerous cylindrical specimens additively manufactured in 0°, 45°, and 90° orientation. Micrographs reveal a non-directional NLγ+β_o microstructure consisting of lamellar α_2/γ colonies, globular γ, and β_o-phase. It is shown, that the microstructure possesses no directional dependence for any specimen. Tensile tests are performed at RT, 300 °C and 850 °C with samples in PBF-EB/M state and after hot isostatic pressing. The tensile tests show a room temperature ductility of up to 2.1% and high temperature strength around 380 MPa. Additionally, a minimum creep rate of 1.0×10^{-8} s^{-1} can be derived from the creep tests at 750 °C with 150 MPa load.

1. Introduction

Gamma titanium aluminides (γ-TiAl) display high strength, high stiffness, good oxidation resistance and good creep properties at elevated temperatures combined with a low density of around 4 g/cm^3 [2–4]. Consequently, γ-TiAl are interesting for high temperature applications in the automotive and aerospace industry [4–6]. They can operate and replace heavier Ni-base superalloys (density about 8 g/cm^3) in jet engines up to service temperatures of 750 °C to reduce fuel consumption, emissions and noise [4,6]. However, the processing and machining of γ-TiAl is challenging due to the low ductility and low fracture toughness at room temperature (RT) [2–4]. Conventional processing technologies like centrifugal casting or isothermal forging followed by hot isostatic pressing (HIP) and heat treatment (HT) are expensive and resource consuming [4]. Therefore, new processing technologies like powder bed fusion (PBF) are investigated. Laser based powder bed fusion (PBF-LB/M) shows several disadvantages when it comes to the processing of γ-TiAl. For example, the increased oxygen pick up, which is caused by the powder production (inert gas atomization) and the PBF-LB/M process itself, embrittles the γ-TiAl [7,8]. Parts produced via PBF-LB/M are characterized by an oxygen content of > 1000 ppm even for fresh powder. Recent heating technologies developed for PBF-LB/M enable process temperatures above the brittle to ductile transition temperature (BDTT) of γ-TiAl and therefore the manufacturing of crack free samples at the expanse of increased Al-evaporation (> 1.2 wt%), provoking changes in chemical composition and subsequently in as-built microstructure and mechanical properties [7]. For temperatures below BDTT, the PBF-LB/M technology leads to cold cracking especially for thick-walled parts [8]. In contrast, the electron based powder bed fusion (PBF-EB/M) with building temperature around 1000 °C and a high vacuum atmosphere

* Corresponding author.
E-mail address: marcel.reith@nmfgmbh.de (M. Reith).

https://doi.org/10.1016/j.mtla.2020.100902
Received 22 June 2020; Accepted 13 September 2020
Available online 19 September 2020

(10^{-3} mbar) with controlled helium inlet provides ideal conditions to build crack-free samples without impurities [9–14]. Additionally, the coarser powder sizes used in PBF-EB/M pick up less oxygen during atomization compared to PBF-LB/M and the process is more cost and resource efficient than conventional processing technologies [15].

Historically, the first γ-TiAl show a poor workability due to the low room temperature ductility. In order to improve the ductility, binary γ-TiAl-alloys with a high Al-content of 48 at.% are identified, showing the best plastic fracture strain at RT [16]. The addition of chromium (Cr) to binary γ-TiAl improves the ductility further [17]. Refractory metals like niobium (Nb), molybdenum (Mo) or tungsten (W) are added to increase oxidation resistance, high temperature strength and creep resistance [18]. In this fashion, 2nd generation γ-TiAl alloys were developed. The well-known GE-alloy Ti–48Al–2Cr–2Nb (Ti-48–2–2) achieves plastic elongations of up to 3% after heat treatment [19]. However, most of these peritectic solidifying 2nd generation alloys operate only up to 700 °C [6].

In order to increase the operating temperature, 3rd generation of γ-TiAl alloys were developed, such as the TNB alloy, which contains 5–10 at.% Nb and small amounts of B and C. The so-called TNM alloy (Ti–43.5Al–4Nb–1Mo–0.1B) is already a process-adapted TiAl alloy, where the properties are specifically tailored to its manufacturing process. The alloy elements Nb and Mo stabilize the β-phase, making it easier for Al lean alloys to solidify through the β-phase field (Fig. 1) [18,20]. β-solidifying alloys possess a less tendency to form segregations and textures during solidification than peritectic alloys [18,20]. Moreover, the widened β-phase field allows a good hot workability of the TNM alloy [20]. The high temperature strength and creep properties are improved by Nb and Mo due to diminished diffusion in the α- and γ-phase [18,20]. The addition of boron and thus the formation of borides has a grain refining effect during solidification and limits the grain coarsening during heat treatment [18,20]. Therefore, the TNM alloy can operate up to 750 °C and was introduced as low pressure turbine (LPT) blade into the geared turbofan (GTF) jet engine in 2016 [6,21].

However, the TNM alloy, which offers the technical feasibility of advanced hot isothermal forging and near conventional hot-die forging, is not as well suited for the PBF-EB/M process. Nb and Mo promote the presence of β_o-phase at room temperature [18,20]. Although the amount of embrittling β_o-phase can be reduced by heat treatment, a room temperature ductility of maximum 1.16% after heat treatment is achievable [22]. In addition, β-solidifying γ-TiAl alloys, similar to Ti–6Al–4 V, have a tendency to form textures (formation of primary β-grains across several melting layers) during the PBF-EB/M process [14,23].

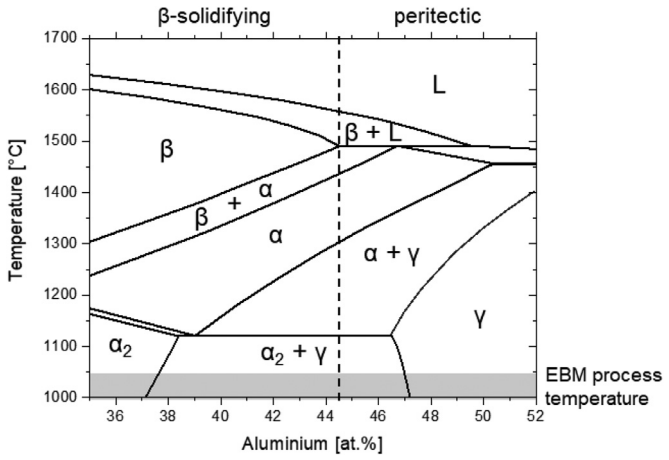

Fig. 1. Binary Ti–Al phase diagram according to Schuster et al. [1]. While the α-grains in β-solidifying alloys, for instance TNM, form from the parental β-phase, the α-phase in peritectic alloys, e.g. Ti-48–2–2, also precipitates directly from the liquid melt.

In order to exploit the full potential of electron beam powder bed fusion, novel γ-TiAl alloys suitable for PBF-EB/M were developed by the Department of Materials Science at the Montanuniversität Leoben (MUL) in cooperation with MTU Aero Engines AG [24–26]. One promising γ-TiAl alloy with the nominal composition Ti–47.5Al–5.5Nb–0.5 W (at.%), called BMBF3, was developed and mechanically characterized in the framework of an ongoing BMBF project 03XP0088C. The high amount of aluminum (47.5 at.%) should improve the room temperature ductility compared to the TNM alloy and the peritectic solidifying constitution is chosen to avoid the formation of textures [14]. In order to maintain the high temperature strength and creep properties of the TNM alloy compared to 2nd generation γ-TiAl, the amount of niobium is increased and molybdenum is substituted by tungsten. While the alloy design should enable good high temperature properties with sufficient room temperature ductility, optimized PBF-EB/M process parameters are necessary to ensure these properties to be homogenous and directional independent.

The feasibility of processing γ-TiAl by PBF-EB/M is shown for several γ-TiAl alloys [9,11,12,14,27]. For instance, electron beam powder bed fused 2nd generation γ-TiAl parts are used for the application in the GE9X jet engine [28]. However, the maximum operation temperature of the Ti-48–2–2 alloy is limited to 700 °C [6]. Therefore, investigating electron beam powder bed fusion of 4th generation γ-TiAl alloys is necessary to exploit the full potential of γ-TiAl. Nevertheless, some challenges, which come along with the PBF-EB/M process, have to be overcome.

The electron based powder bed fusion process can be basically divided into four steps. First the build platform is lowered by the amount of one layer, followed by the application of powder via a rake system. In the third step, called heating, the powder is sintered by a defocused electron beam to prevent smoke events during melting. The heating step is also used to adjust the build temperature. Finally, the areas specified by the sliced CAD model are melted with a focused electron beam. For a more detailed description of the PBF-EB/M process and the materials used the reader is referred to [29].

Poorly optimized parameters, especially for heating and melting, can lead to defects attributed to the PBF-EB/M process. These defects are classified as cracks, misconnections, and gas pores. Cracks align predominantly in the building direction and are avoided by a high building temperature. Misconnections are characterized by a thin, elongated shape with sharp edges (see Fig. 2) and occur between the melting layers due

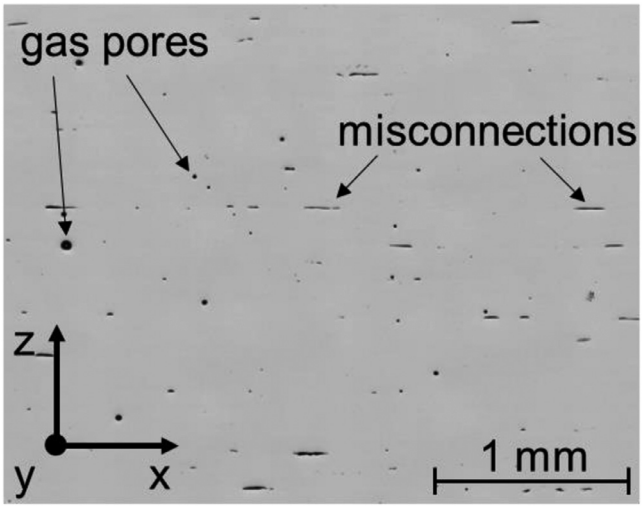

Fig. 2. Defects attributed to the PBF-EB/M process for poorly optimized parameter. Misconnections align perpendicular to the build orientation (= z-orientation) between two layers, if the melting is insufficient. They are characterized by an elongated shape with sharp edges, whereas gas pores are spherical and randomly distributed.

to a lack of fusion. Misconnections can be minimized by increasing the energy input during the melting step [9,11,12]. However, a very small residual amount of misconnection can never be eliminated for certain as a result of statistical errors. Gas pores remain in the microstructure if the melt pool solidifies before the gas can ascend to the surface. Gas pores are introduced into the melt pool by powder particles with entrapped gas [30], cavities between the powder particles [31] or a turbulent melt pool [32].

These defects diminish the mechanical properties and can even outweigh the influence of the microstructure [33]. γ-TiAl are particularly prone to misconnections because of their low fracture toughness [34,35]. Depending on the orientation of the specimen, misconnections have a different influence on the room temperature ductility of γ-TiAl [36]. Misconnections aligned perpendicular to the loading direction act like notch tips due to their sharp edges, which results in premature failure. In contrast, the impact of misconnections aligned parallel to the loading direction is less severe [36].

In addition, a heterogenous microstructure can form during the PBF-EB/M process. At room temperature the microstructure of γ-TiAl consists mainly of two ordered phases, the face-centered tetragonal γ-phase and the hexagonal α_2-phase [2,18]. In modern γ-TiAl alloys, for example the TNM alloy, the body-centered cubic β_o-phase can also occur [37]. Depending on the composition and thermal history, four different microstructures exist: near-gamma, duplex, nearly-lamellar and fully lamellar [2]. Several studies are focusing on the γ-TiAl microstructure in particular the formation of inhomogeneities. Todai et al. observed a layered microstructure composed of coarse grained γ-bands and duplex-like regions [13]. Klassen et al. and Baudana et al. relate the appearance of heterogeneity to PBF-EB/M specific peak temperatures and local overheating leading to Al-evaporation [38,39]. Obviously, a heterogeneous microstructure influences the mechanical properties [13].

Both, defects and a layered microstructure, can lead to anisotropic mechanical properties. Experimental results regarding the impact of inhomogeneities and accordingly specimen orientation on mechanical properties are provided by [13] and [36] for Ti–48Al–2Nb–2Cr. Yield strength and tensile strength vary between 560–605 MPa and 610–700 MPa, respectively [13,36]. A more significant change is observed for the elongation at fracture at RT, where vertically aligned samples respond more sensitive to misconnections than horizontal ones. Both, Jüchter and Todai et al., observed less than 1.0% elongation at fracture for vertically aligned samples, while horizontal ones display significantly increased values up to 2.5% elongation at fracture [13,36]. Anisotropic mechanical properties are not only harmful for a vast scope of applications but also affect the machining of electron beam powder bed fused γ-TiAl parts, which is necessary for high quality surfaces required by the automotive and aerospace industry.

In the following, the Ti–47.5Al–5.5Nb–0.5 W alloy specifically designed for PBF-EB/M is processed with optimized parameters. While the composition of the Ti–47.5Al–5.5Nb–0.5 W alloy provides good high temperature properties with sufficient RT ductility and a peritectic solidification path to avoid textures, the focus of this work is on the optimization of the PBF-EB/M process parameters for minimized defects and a homogenous microstructure, leading to directional independent mechanical properties, which are evaluated by tensile and creep tests.

2. Experimental

The primary Ti–47.5Al–5.5Nb–0.5 W (at.%) rods are produced by *GfE Metalle und Materialien GmbH (Nuremberg, Germany)*. The rods are then gas atomized into spherical powder with a particle size distribution from 50 µm to 120 µm by *TLS Technik GmbH & Co. Spezialpulver KG* (*Bitterfeld, Germany*). The produced powder with the chemical composition Ti–47.48Al–5.55Nb–0.42 W (at.%) is processed on an *Arcam A2X* (*Arcam AB, Mölndal, Sweden*) with the software version *EBM Control 5.2*. The samples for defect and microstructure examination are grinded and afterwards polished with a suspension consisting of 50 ml OPS, 50 ml distilled water, 10 mg KOH, and 10 ml 30% H_2O_2. Light microscopy images for defect analysis are taken on a *Zeiss AxioImager.M1m* (*Carl Zeiss AG, Jena, Germany)*. The defect density is examined at six positions (approx. 10 mm, 30 mm, 40 mm, 60 mm, 70 mm and 90 mm build height) of two vertically aligned cylinders per build job as well as on the remaining portions of the cylinders built for tensile testing (see Fig. 3, left). The area fraction of cracks, misconnections, and gas porosity in the light microscopy images is evaluated by an automated script.

Images of the microstructure are taken with the scanning electron microscope (SEM) *Helios NanoLab 600i* (*FEI Company, Hillsboro, Oregon, USA*) with a *circular backscatter electron detector* (CBS). These SEM pictures are used to determine the grain size by a linear intercept method. Phase fractions of the manufactured samples are analyzed by *X-ray diffraction (XRD)* on a *Bruker D5000* (*Bruker Corporation, Billerica, Massachusetts*). The measurement of the Al-content via *X-ray fluorescence spectroscopy (XRF)* is conducted by *GfE Metalle und Materialien GmbH (Nuremberg, Germany)*.

76 cylindrical specimens with a diameter of 12 mm and a length of 90 mm are built vertically (0°, 28 samples), diagonally (45°, 24 samples) and horizontally (90°, 24 samples) as shown in Fig. 3 on the left. Half of the cylinders are hot isostatic pressed at 1225 °C with 100 MPa for 4 h by *Bodycote* (*Munich, Germany*). Samples for tensile tests are machined

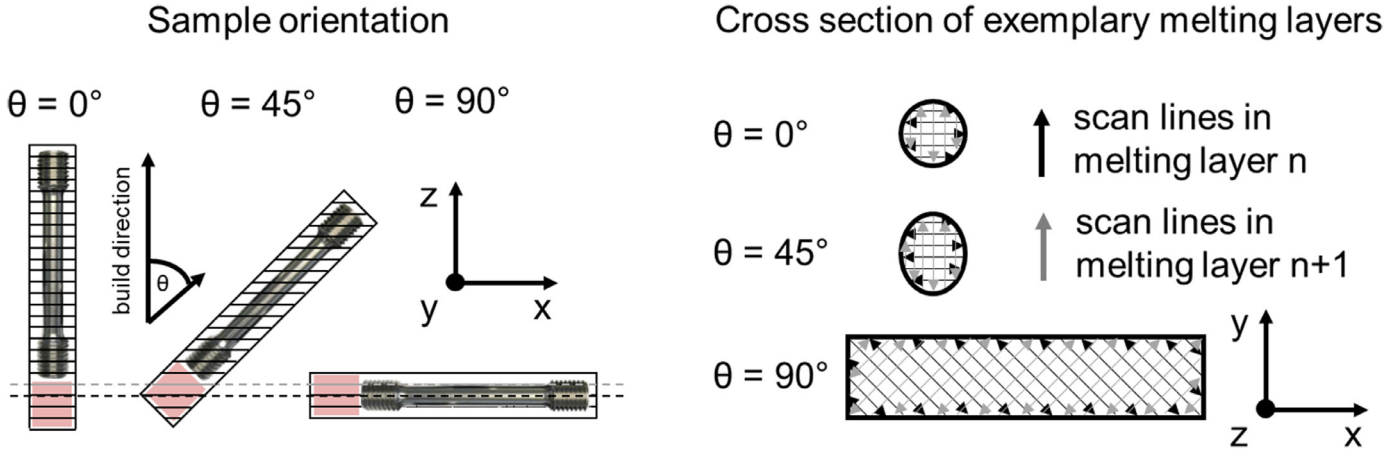

Fig. 3. On the left side the building layers in differently oriented cylinders are shown. The cylinders are built vertically (0°), diagonally (45°) and horizontally (90°). The remaining portions for defect examination are indicated red. The scan lines of the two marked melting layers on the left side, are shown by black and gray arrows on the right side. The hatching strategy of the first layer n (black) are rotated by 90° in the subsequent layer $n+1$ (gray).

to the final dimensions showing a gauge length of 25 mm and a diameter of 5 mm. The tensile tests are conducted on a *Zwick&Roell Z100* (*Zwick Roell AG, Ulm, Germany*) at room temperature, 300 °C, and 850 °C. The strain rate of the tensile test is 0.0001 s^{-1}, which is accelerated after a plastic strain of 4% to 0.0003 s^{-1} for practical reasons. The tensile specimens and test conditions are according to the limits of DIN EN ISO 6892 [40]. Each test condition is based on three tensile specimens. In exceptional cases, only two specimens are available due to errors during machining or testing. The tension creep experiments are conducted on an *ATS 2330* (*Applied Test Systems, Butler, USA*) at 750 °C with a constant load of 150 MPa. The specimens are machined to a gauge length of 30.5 mm and a diameter of 5.3 mm. The tests are conducted conform to DIN EN ISO 204 [41]. The creep tests are stopped after either 1% strain or 200 h, whichever is reached first.

The cylindrical specimens are manufactured via PBF-EB/M with a layer thickness of 100 µm and a building temperature above 1000 °C. Cross-snake is the chosen hatching strategy and the beam orientation is rotated by 90° per layer (see Fig. 3, right). All specimens are built without contour.

Due to the varying scan length (L_{scan}) in the cylindric samples (Fig. 3, right) the beam power (P_{scan}) and velocity (v_{scan}) have to be adjusted to ensure constant melting conditions. Two main criteria have to be met:

1) Energy input = P_{sacn} / (v_{scan} * l_{offset}) = P_{ref} / (v_{ref} * l_{offset}) = const.
2) Mean beam return time = L_{scan} / v_{scan} = L_{ref} / v_{ref} = const

The velocity adjustment can be derived from criteria 2.

$$v_{scan} = v_{ref} * L_{scan}/L_{ref}$$

To ensure a constant energy input while the line offset (l_{offset}) is kept constant, the beam power has to be adjusted according to the velocity.

$$P_{scan} = P_{ref} * v_{scan}/v_{ref} = P_{ref} * L_{scan}/L_{ref}$$

The reference parameter set in this work is determined on cubes with an edge length of 15 mm. For these cuboids with scan lengths of 15 mm (L_{ref}) the reference beam power is set to 510 W (P_{ref}) and the reference velocity equates to 4000 mm/s (v_{ref}). The line offset is 0.075 mm and thus the area energy is 1.7 J/mm.

3. Results

3.1. Microstructure

All samples show a NLγ+β_o microstructure consisting of lamellar α_2/γ areas, globular γ-phase, and β_o-phase. In Fig. 4 all characteristic microstructure features are marked in an exemplary NLγ+β_o microstructure. The total Al loss due to the PBF-EB/M process is determined to be between 0.7 wt% and 0.8 wt%.

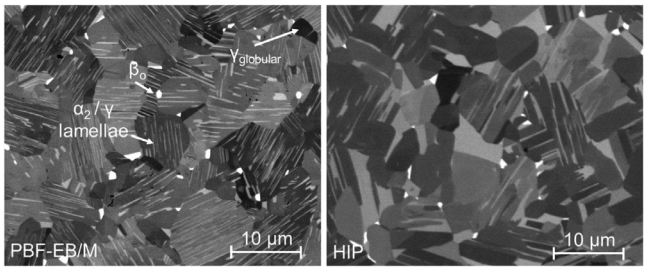

Fig. 4. NLγ+β_o microstructure of PBF-EB/M specimen (left) and HIP specimen (right), consisting of lamellar α_2 /γ areas (α_2 lighter grey, γ darker grey), globular γ-phase (dark grey), and β_o-phase (white).

Table 1
The grain size is determined by a linear intercept method in SEM images. All samples show equiaxed grains with grain sizes of approximately 4.5 µm in PBF-EB/M and around 5.0 µm in HIP condition.

Grain size	Vertical (0°)		Diagonal (45°)		Horizontal (90°)	
	X	*Z*	*X*	*Z*	*X*	*Z*
PBF-EB/M	4.8 µm	4.5 µm	4.9 µm	5.0 µm	4.7 µm	4.2 µm
HIP	5.7 µm	4.4 µm	5.5 µm	5.0 µm	5.2 µm	4.9 µm

The microstructure does not change over the building height as shown for a vertical cylinder at build heights of 10 mm and 60 mm (Fig. 5). Moreover, the build orientation has no influence on the microstructure as well (see Fig. 6, left). The PBF-EB/M specimens of all three build orientations (vertical, diagonal and horizontal) possess comparable grain sizes between 4.2 µm and 5.0 µm (Table 1). Further, all samples show equiaxed grains characterized by small variations of the grain size between x- and z-direction (= building direction). Lastly, no textures or layers are observed in any specimen.

After the hot isostatic pressing the microstructure consists of the same features (Fig. 6, right) and hence is still characterized as NLγ+β_o. The three build orientations (vertical, diagonal and horizontal) show similar grain sizes. The grains are not strongly elongated in *x*- or *z*-direction. However, the grains slightly coarsen during HIP (Table 1). In average the grains are 0.4 µm coarser than after the PBF-EB/M process.

Four exemplary XRD patterns are shown in Fig. 7. The position and intensity of the peaks are not impacted by the build orientation or the HIP process. Therefore, all tested samples show the same phases

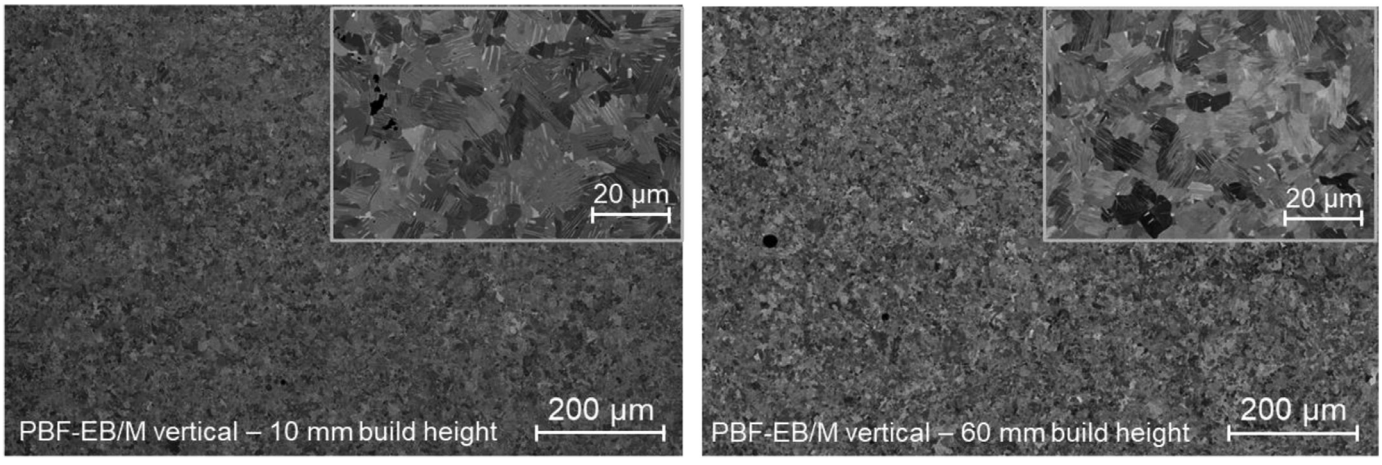

Fig. 5. SEM-CBS microstructure images taken at 10 mm and 60 mm build height with lamellar α_2/γ areas (α_2 lighter grey), globular γ (dark grey) and β_o-phase (white).

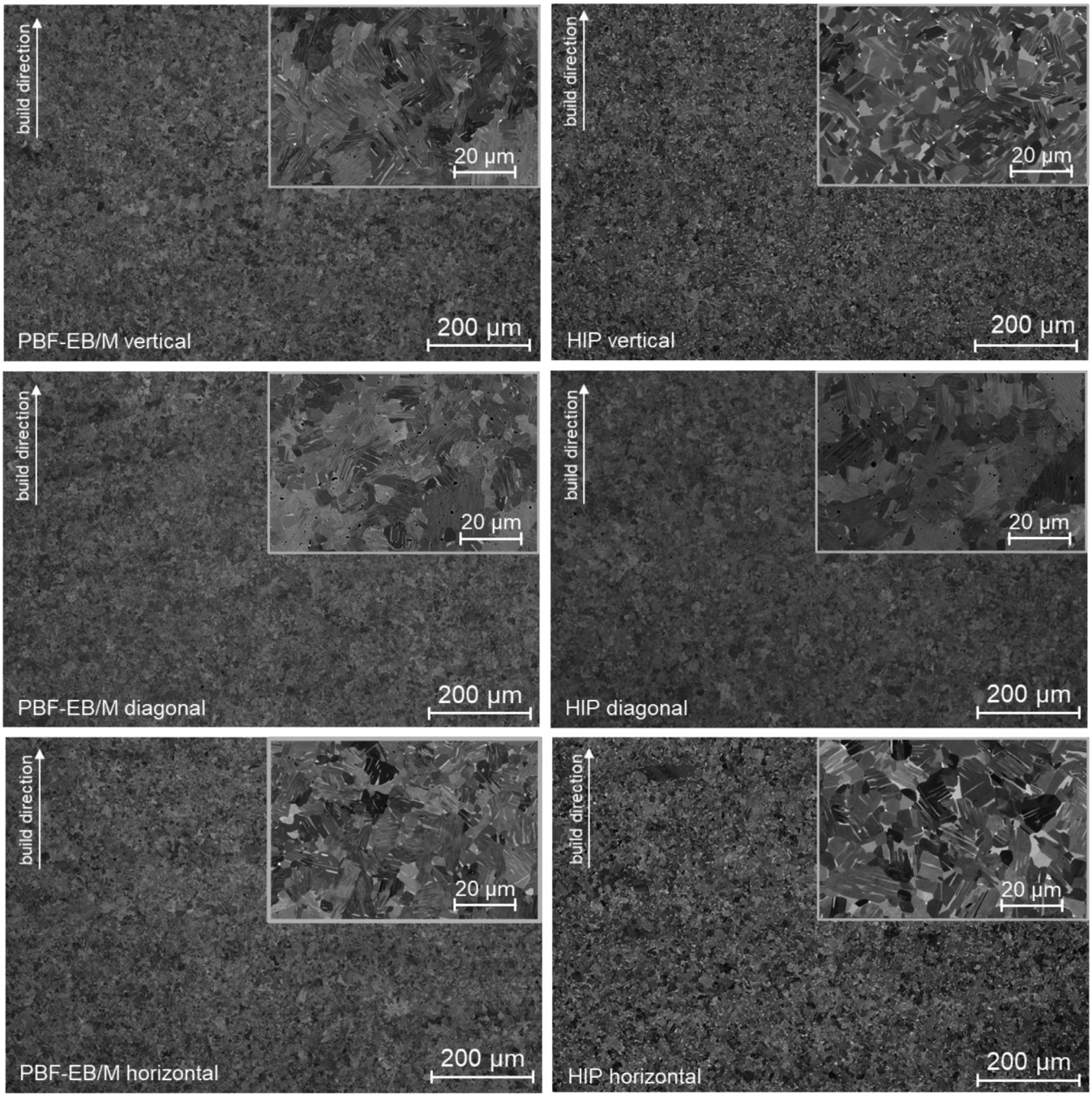

Fig. 6. SEM-CBS images in PBF-EB/M condition (left) and after HIP (right). The microstructure is shown for vertical (0°, top), diagonal (45°, middle) and horizontal (90°, bottom) specimen. It consists of lamellar α_2/γ areas (α_2 lighter grey), globular γ (dark grey) and β_o-phase (white). The black dots are residuals of the polishing agent.

and same phase fractions within the resolution of the XRD device. The overall content of α_2- and γ-phase in all samples is 8.5 ± 0.8 wt% and 91.5 ± 0.8 wt%, respectively. The phase fraction of β_o-phase is below the resolution of the XRD-device. Although most of the microstructure consists of γ-phase, the XRD measurements give no indication if the γ-phase is present as globular γ or within lamellar colonies. The orientation of the sample and the HIP process have no influence on the phase fraction.

3.2. Defects

In order to assure the quality of the built cylinders, two vertical cylinders from each of the two build jobs are investigated at six positions divided equally over the total height of the build. Moreover, the remaining portions of 15 samples from tensile tests are examined (as shown in Fig. 3). The average values over all tested samples are listed in Table 2.

Table 2
Misconnections and gas porosity averaged over all tested cylinders in the PBF-EB/M and with additional HIP.

defect	PBF-EB/M	HIP
misconnections	0.006% ± 0.003%	0.001% ± 0.001%
gas porosity	0.249% ± 0.047%	0.002% ± 0.002%

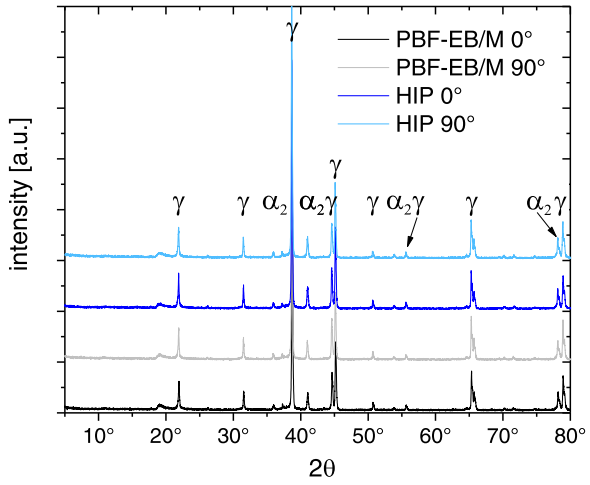

Fig. 7. XRD-measurements for one vertical (0°) and one horizontal (90°) cylinder in PBF-EB/M condition and after HIP. The peaks of each measurement are similar, showing no influence of the build orientation and HIP on the phase fraction of α_2- and γ-phase.

Both, misconnections and gas porosity, are on a constant level independent of sample orientation, built height, and build job. By hot isostatic pressing the misconnections can be further reduced. In addition, the gas porosity reaches a similarly low level as the misconnections (Table 2 and Fig. 8).

3.3. Mechanical properties

The mechanical properties from tensile tests at room temperature, 300 °C, and 850 °C are shown in Fig. 9.

Direction-independence is observed for the yield strength at room temperature (750 MPa ± 10 MPa), 300 °C (680 MPa ± 10 MPa), and 850 °C (390 MPa ± 10 MPa) regarding PBF-EB/M conditions. The tensile strength indicates a direction-independent behavior, too. Regardless of orientation, the tensile strength of PBF-EB/M samples decreases from 795 MPa (± 15 MPa) at room temperature to 430 MPa (± 10 MPa) at 850 °C. Yield strength and tensile strength, which were examined on hot isostatic pressed samples, also give no indication of a directionality.

In contrast, the elongation at fracture indicates a small anisotropy for PBF-EB/M samples at RT. Vertically aligned specimen provide less than 0.8% (± 0.1%) while horizontal ones provide up to 1.2% (± 0.5%) elongation at fracture. After HIP the ductility at RT is improved and the directional dependence is eliminated considering the large scattering of the results. The tensile tests at 300 °C show similar results as at RT at a higher level. At 850 °C the elongation at fracture is independent of the built direction for both conditions, PBF-EB/M and HIP, with each sample achieving at least 30% elongation at fracture. Nevertheless, experimental derived values for the elongation at fracture are characterized by a striking large scatter which reveals the sensitivity of γ-TiAl for defects.

Exemplary curves of the tensile creep experiments at 750 °C with 150 MPa load are shown for PBF-EB/M and HIP condition in Fig. 10. In both conditions, the microstructure is characterized as NLγ+β_o, but the HIP microstructure is comparatively coarse (Table 1). The 0°, 45°, 90° test specimens possess similar curves in each condition, respectively. However, the slope of the HIP creep curves is flatter than for PBF-EB/M samples. The minimum creep rate is determined in the linear section of the creep curves between 50 h and 150 h. The average minimum creep rate and the corresponding standard deviation are plotted in Fig. 10 for 0°, 45° and 90° orientation. The minimum creep rate is neither in the PBF-EB/M state, nor after hot isostatic pressing influenced by the orientation of the samples. After HIP the minimum creep rate is slightly smaller and thus the samples are more creep resistant.

After the tensile creep tests, the samples still show a NLγ+β_o microstructure (Fig. 11) similar to the initial microstructure (Fig. 4). Neither grain deformation, nor formation of new grains is observed in any specimen. However, the amount of β_o phase seems slightly reduced.

4. Discussion

4.1. Defects and microstructure

The used scan strategy with an area energy of 1.7 J/mm^2 lead to misconnections ≤ 0.006%, gas porosity ≤ 0.25% as well as an aluminum loss ≤ 0.8 wt%. The measured amount of misconnection is caused by statistical errors of the additive manufacturing process and is classified as an unpreventable event. The remaining gas porosity of 0.25% is in the same range as available data from recent publications, reporting porosities below 0.5% [11,13,38]. It is important to note, that the porosity can be further reduced at the expense of increased Al evaporation by increasing the energy input. The experimentally derived aluminum loss of ≤ 0.8 wt% deviates to a large extent from data of previous studies. *Baudana* et al. and *Todai* et al. revealed a typical aluminum loss of 1.7 wt% – 2.1 wt%. Minimizing the aluminum loss ensures the formation of a homogeneous microstructure for both, PBF-EB/M and HIP conditions (Fig. 6).

Basically, the solidification rate is determined by the difference between peak temperature of the melt pool and the building temperature. Due to the recurrent heating step the building temperature at the surface is constantly around 1000 °C, independent of the part geometry. Because of the scan length adjusted melting parameter (constant energy input and return time) and similar hatching strategies (Fig. 3) the peak temperature of each sample is similar. An increase of the peak temperature would enhance the aluminum evaporation [39], while a higher solidification rate would result in a finer microstructure. Neither of both is observed for any sample. Moreover, the specimens are located in a sinter cake for several hours slightly below 1000 °C. Therefore, the specimens are in-situ heat treated inside the α_2- and γ-phase field. As a result, all samples show a similar grain size (Table 1) with nearly equiaxial grains (Fig. 6). Furthermore, all tested samples have the same amount of α_2+γ phase, as revealed by the XRD-measurements (Fig. 7). Additionally, the peritectic solidification path of the Ti–47.5Al–5.5Nb–0.5 W alloy avoids the formation of a texture as observed for the β-solidifying TNM alloy [14]. Consequently, the PBF-EB/M process parameter developed for the Ti–47.5Al–5.5Nb–0.5 W alloy enables a homogenous microstructure without layers not only within one specimen, but for all specimens independent of the building orientation or build height.

The HIP process (1225 °C) and the PBF-EB/M process (1000 °C) are operating in the α+γ and the α_2+γ phase field at similar temperatures. The slightly increased temperature of the HIP process provokes grain coarsening without notably changing the phase fractions of α_2 and γ phase compared to the PBF-EB/M samples.

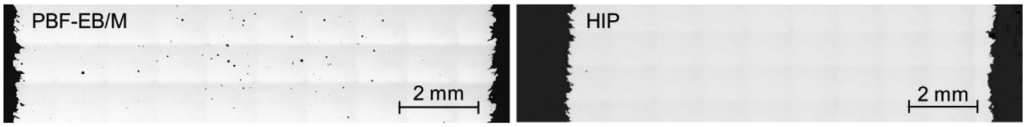

Fig. 8. Light microscopic image of a vertically aligned cylinder in PBF-EB/M state (left) and after HIP (right).

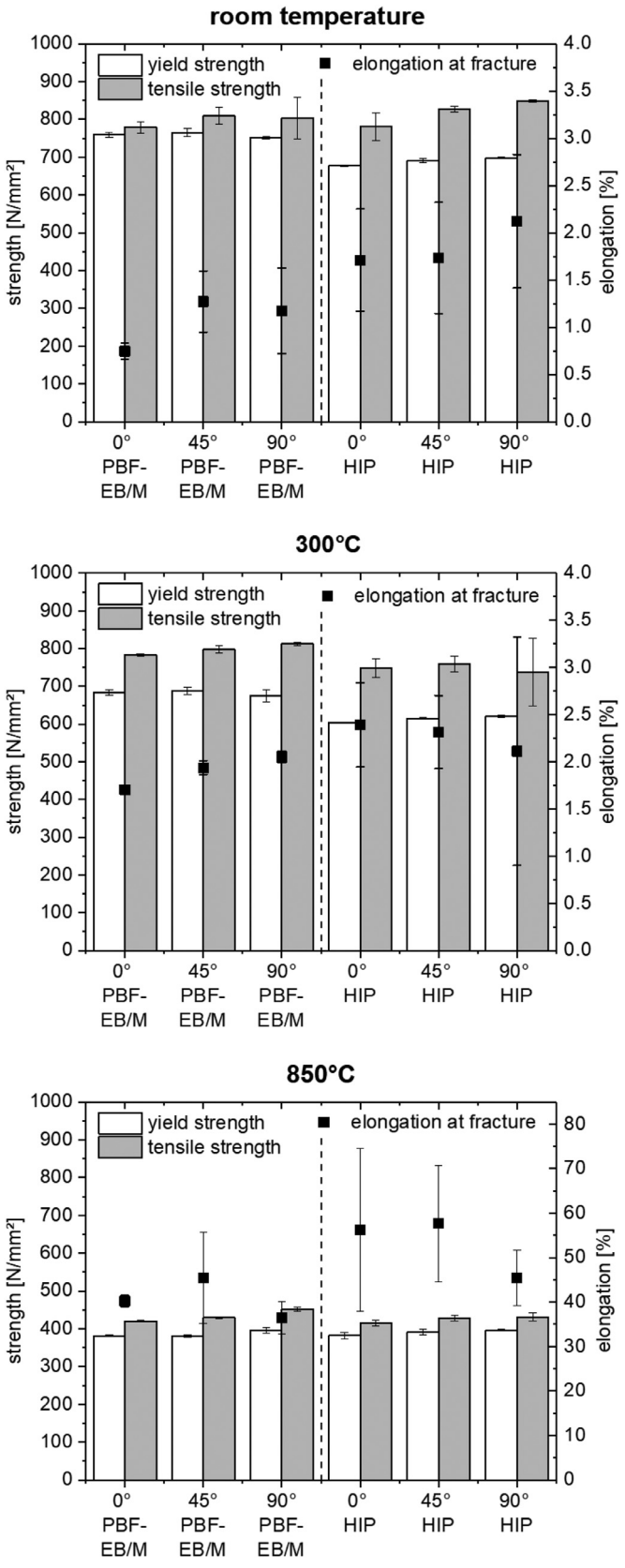

Fig. 9. Mechanical properties obtained from tensile tests of PBF-EB/M and HIP specimnes in dependence on temperature and orientation.

4.2. Mechanical properties

Tensile tests as well as creep tests indicate promising mechanical properties almost independent from specimen orientation for both conditions, PBF-EB/M and HIP. The mechanical properties of the Ti–47.5Al–5.5Nb–0.5 W alloy are compared to a 2nd generation Ti–48Al–2Nb–2Cr alloy (Ti-48–2–2), which is currently used for PBF-EB/M turbine blades (operating temperatures up to 700 °C) in the GE9X engine [6,28], as well as to Ti–43.5Al–4Nb–1Mo–0.1B alloy (TNM) in cast/HIP condition, which can operate 50 °C higher than Ti-48–2–2 [6,21]. An overview of the room temperature properties is given in Fig. 12.

Directional independence of yield and tensile strength is achieved by the homogeneous microstructure with minimized defects. Particularly the isotropic yield strength confirms that all samples possess an almost identical microstructure. The directional independence is demonstrated by a constant level at various temperatures for both, PBF-EB/M and HIP condition (Fig. 9).

The 750 MPa yield strength (YS) at RT, achieved by the NLγ+β_o microstructure of the Ti–47.5Al–5.5Nb–0.5 W alloy, is superior to PBF-EB/M manufactured Ti-48–2–2 with duplex (350 MPa [9]) and layered microstructure (580–600 MPa [13]). The TNM alloy (cast + HIP condition) is characterized by a nearly lamellar microstructure and a yield strength at RT of less than 700 MPa [22].

During hot isostatic pressing the microstructure of the Ti–47.5Al–5.5Nb–0.5 W alloy coarsens slightly (Table 1), leading to wider α_2/γ lamellae and less phase interfaces. Therefore, the mobility of dislocations in the material is improved [18,43], resulting in a reduction of the yield strength. After the HIP process the YS of the alloy is on a similar level as the cast + HIP TNM alloy.

The YS of the Ti–47.5Al–5.5Nb–0.5 W alloy at 300 °C shows similar results as at RT. However, all values are reduced by around 50 MPa because the dislocation movement is enhanced by the elevated temperature.

At 850 °C the brittle to ductile transition temperature (BDTT, typically around 700 °C for engineering γ-TiAl [6]) of the alloy is exceeded, leading to a reduction of the yield strength from 750 MPa to 380 MPa. Due to this ductile behavior, the coarser microstructure after HIP has no influence on the yield strength above the BDTT. The 380 MPa YS is still better than duplex Ti-48–2–2 (330 MPa [9]) and similar to layered Ti-48–2–2 (390 MPa [13]). The YS of the cast + HIP TNM alloy is about 460 MPa [22]. However, it has to be noted that the mechanical properties of Ti-48–2–2 and TNM are measured at 800 °C (lower testing temperature should lead to higher yield strength).

The trends observed for the yield strength can also be applied to the tensile strength.

The elongation at fracture is more sensitive to misconnections than the yield or tensile strength due to the low ductility and fracture toughness of γ-TiAl [36]. Therefore, the isotropy of the mechanical properties can be assessed best for the elongation at fracture. The sensitivity at room temperature can be confirmed by the large scatter with only three samples available per orientation and condition. Further, the scatter is influenced by the alignment of the tensile test setup along the z-axis, which is not additionally calibrated prior to the test. This could lead to minimum bending loads and thus diminish the mechanical properties as well as increase the scatter of the results.

At room temperature, the PBF-EB/M specimens of the Ti–47.5Al–5.5Nb–0.5 W alloy show a directional dependence of the elongation at fracture. The microstructure of these specimens is homogeneous without a texture or layers. All samples independent of the build orientations show similar phase fractions with equiaxed grains of comparable size. Therefore, the microstructure should have no influence on the ductility, which is supported by the directional independent yield strength. Consequently, the anisotropic ductility is probably caused by a combination of the statistical occurring misconnections (< 0.01%) and the low fracture toughness of titanium aluminides. The elongated misconnections with sharp edges inside the vertical samples are oriented perpendicular

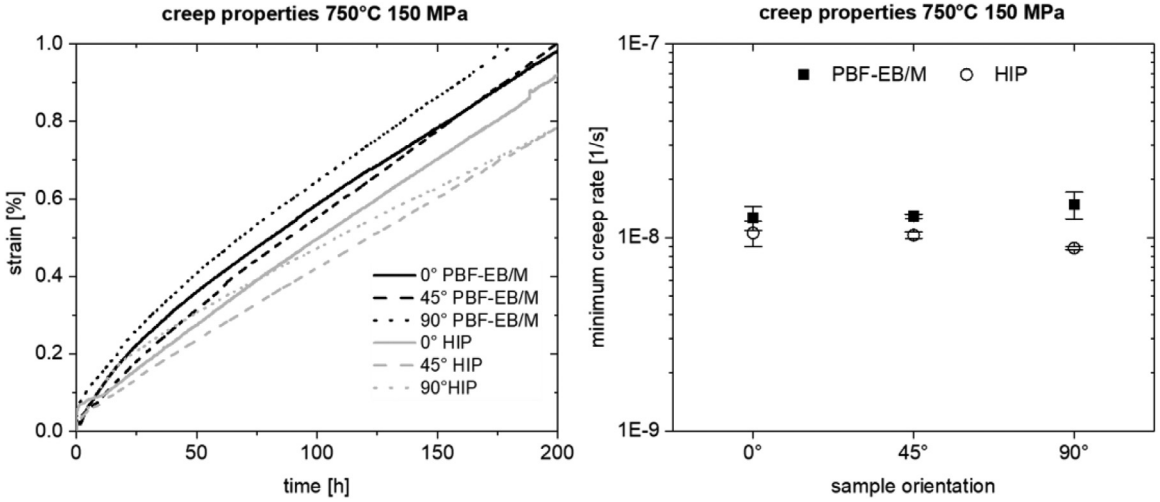

Fig. 10. Tension creep tests at 750 °C with 150 MPa load. Left: Strain is plotted over time. Right: Minimum creep rates in dependence of specimen orientation.

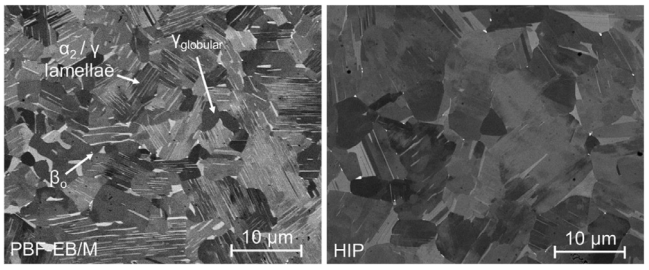

Fig. 11. NLγ+β_o microstructure of two exemplary samples after tensile creep tests at 750 °C with 150 MPa load. In both conditions, PBF-EB/M (left) and HIP (right), the microstructure is characterized as NLγ+β_o, but the HIP microstructure is comparatively coarse.

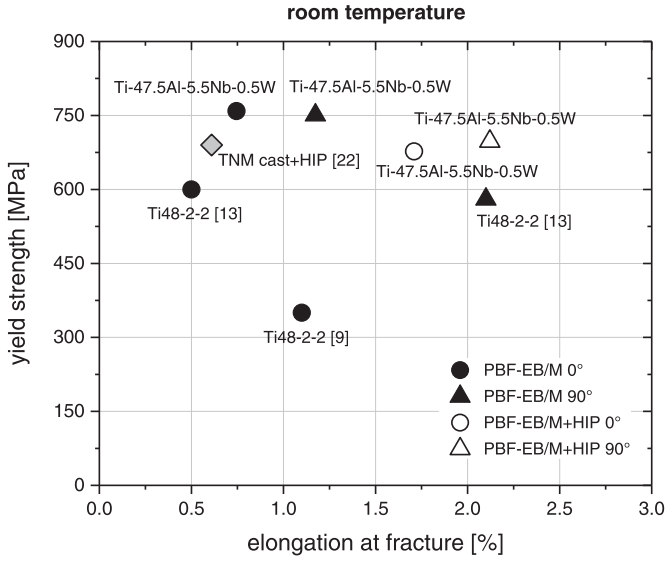

Fig. 12. The yield strength and the elongation at fracture of the Ti–47.5Al–5.5Nb–0.5 W alloy is compared to 2nd generation Ti–48Al–2Nb–2Cr (Ti48–2–2) and Ti–43Al–4Nb–1Mo–0.1B (TNM) at room temperature.

to the loading direction, leading to an increased stress and hence failure. In the diagonal and horizontal specimens, the misconnections are oriented less critical and the stress increase is smaller. Similar results are shown by *Jüchter* for duplex Ti-48–2–2 [36].

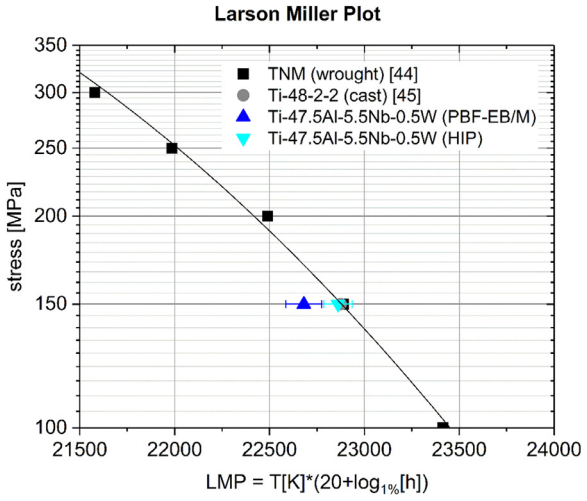

Fig. 13. Larson Miller Plot for 1% strain during tensile creep tests. The Ti–47.5Al–5.5Nb–0.5 W alloy is tested in PBF-EB/M and HIP condition with a NLγ+β_o microstructure, while the wrought TNM alloy shows a NL+γ microstructure and the cast Ti–48Al–2Nb–2Cr alloy has a mainly lamellar microstructure with equiaxed regions.

The samples of the Ti–47.5Al–5.5Nb–0.5 W alloy possess an elongation at fracture of 0.8% vertically and 1.2% horizontally which is in good accordance with values of duplex Ti-48–2–2, showing an elongation at fracture of 0.7% to 1.5% [9,36]. Ti-48–2–2 with a layered microstructure shows an anisotropy with 0.5% elongation for vertical and 2.2% for horizontal specimens [13]. According to the author, the high ductility of the horizontal samples is achieved by ductile γ-bands, which carry the bulk of the deformation if orientated correctly to the loading direction and hence also cause the anisotropy [13].

After the HIP process, the elongation at RT is on a rather constant level between 1.7% and 2.1% considering the large scatter (± 0.6%). During the HIP process the statistical occurring misconnections are eliminated, leading to a directional independent elongation. This reinforces the previously mentioned theory about misconnections as the root of the anisotropy. In addition, the reduced yield strength due to grain coarsening, enhances the plastic deformation and hence weakens the sensitivity towards misconnections.

In comparison to the nearly lamellar cast + HIP TNM alloy (0.6% elongation at fracture [22]), the Ti–47.5Al–5.5Nb–0.5 W alloy shows up

to twice the ductility in PBF-EB/M and almost triple the ductility after HIP.

At 300 °C, the ductility of the alloy is slightly increased due to enhanced dislocation mobility, but still shows similar tendencies like at room temperature. However, the anisotropy in PBF-EB/M state is less pronounced and the impact of the hot isostatic pressing is less severe.

At 850 °C all samples of the Ti–47.5Al–5.5Nb–0.5 W alloy show a sufficient elongation at fracture of at least 30% and no direction is favorable.

The creep properties are mainly determined by the microstructure of γ-TiAl. The fully lamellar microstructure possesses the best creep properties due to the increased number of phase interfaces, followed by nearly lamellar microstructure and duplex microstructure, which provides significantly reduced creep properties [2,10,18,42]. A finer lamellar spacing enlarges the phase-interfaces and thus improves the creep properties due to restricted dislocation mobility [18,22,42].

The homogeneous and isotropic microstructure leads to similar creep properties for each direction in both PBF-EB/M and HIP condition, respectively (Fig. 10). The nearly identical minimum creep rate for all three build orientations underlines further, that the microstructure forms no preferred orientations with the used PBF-EB/M parameters. Although the NLγ+β_o microstructure after HIP is slightly coarser (Table 1), the minimum creep rate after HIP (1.0×10^{-8} s^{-1}) is lower than in PBF-EB/M condition (1.4×10^{-8} s^{-1}). The similar microstructure before (Fig. 4) and after (Fig. 11) the tensile creep tests indicates dislocation climb as the main creep mechanism [18,44]. However, a more detailed analysis of the creep mechanisms is subject to further research and goes beyond the scope of this publication. A change in lamellar spacing, which is mainly influenced by the solidification rate, should be investigated as well as the fraction of globular γ-phase. Both have a huge impact on the creep properties [18,22,43]. Nevertheless, the reduced defects after HIP should have no influence on the minimum creep rate, because the high ductility of γ-TiAl above BDTT (creep tensile tests at 750 °C) should allow to compensate small amounts of defects by plastic deformation.

The minimum creep rate at 750 °C with 150 MPa load of the Ti–47.5Al–5.5Nb–0.5 W alloy (1.4×10^{-8} s^{-1}) is similar to the minimum creep rate of casted Ti-48–2–2 with mainly lamellar microstructure (1.5×10^{-8} s^{-1} [45]). After hot isostatic pressing, the minimum creep rate of the Ti-47.5Al-5.5Nb-0.5 W alloy (1.0×10^{-8} s^{-1}) is higher than the cast + HIP TNM alloy with nearly lamellar γ microstructure (7.0×10^{-9} s^{-1} [22]).

The Larson Miller Plot in Fig. 13 compares the tensile creep performance of different γ-TiAl alloys at 1% strain. After HIP, the Ti–47.5Al–5.5Nb–0.5 W alloy with a coarsened NLγ+β_o microstructure shows similar creep properties as the wrought TNM alloy with a NL+γ microstructure [44] and cast Ti–48Al–2Nb–2Cr with a mainly lamellar microstructure [45]. Therefore, the creep properties of the Ti–47.5Al–5.5Nb–0.5 W alloy processed via PBF-EB/M are on a similar level as currently used γ-TiAl with the potential to be further improved by an adjusted lamellar microstructure [18].

5. Conclusion

The novel γ-TiAl alloy (BMBF3) with the nominal composition Ti–47.5Al–5.5Nb–0.5 W (at.%) is specifically designed for the PBF-EB/M process. A well-balanced parameter set to build high quality parts is identified for this 4th generation γ-TiAl alloy and results in a low level of misconnections and a homogeneous microstructure. The remaining gas porosity is a tradeoff for a reduced aluminum evaporation, necessary for the homogeneous microstructure.

Three main goals are accomplished:

1) Isotropic mechanical properties are almost achieved by a homogenous microstructure and the reduction of misconnections to a minimum. At room temperature the elongation at fracture shows small anisotropy.
2) The ductility at room temperature in as-HIP condition is up to 3 times higher than the ductility of the TNM alloy in cast/HIP condition.
3) Simultaneously, the ductile as-HIP PBF-EB/M BMBF3 alloy also maintained the high temperature strength level of the TNM alloy in cast/HIP condition.

Thus, the Ti–47.5Al–5.5Nb–0.5 W combines the high temperature strength of the TNM alloy with the high room temperature ductility of 2nd generation Ti-48–2–2. Furthermore, it enables PBF-EB/M to be a true processing alternative to the challenging and expansive conventional manufacturing process of TNM alloy for applications up to 750 °C operating temperature.

Declaration of Competing Interest

The authors declare that they have no known competing financial interests or personal relationships that could have appeared to influence the work reported in this paper.

Acknowledgment

The authors gratefully acknowledge the funding by the Federal Ministry of Research and Education of Germany (BMBF project 03XP0088C). The multi-annual BMBF project is focusing on alloy development of intermetallic γ-titanium aluminides (TiAl). One promising TiAl-based alloy with the nominal composition Ti–47.5Al–5.5Nb–0.5W (at.%), named BMBF3, is subject of this publication.

References

[1] J.C. Schuster, M. Palm, Reassessment of the binary Aluminum-Titanium phase diagram, J. Phase Equilib. Diffus. 27 (2006) 255–277.
[2] Y.-.W. Kim, Intermetallic alloys based on gamma titanium aluminide, JOM 41 (1989) 24–30.
[3] H. Clemens, W. Smarsly, Light-weight intermetallic titanium aluminides – status of research and development, Adv. Mat. Res. 278 (2011) 551–556.
[4] B.P. Bewlay, S. Nag, A. Suzuki, M.J. Weimer, TiAl alloys in commercial aircraft engines, Mater. High Temp. 33 (2016) 549–559.
[5] T. Tetsui, Application of TiAl in a turbocharger for passenger vehicles, Adv. Eng. Mater. 3 (2001) 307–310.
[6] Y.-.W. Kim, S.-.L. Kim, Advances in gammalloy materials–processes–application technology, JOM 70 (2018) 553–560.
[7] A. Vogelpoth, J.H. Schleifenbaum, S. Rittinghaus, Laser additive manufacturing of titanium aluminides for turbomachinery applications, Ceramics; Controls, Diagnostics, and Instrumentation; Education; Manufacturing Materials and Metallurgy, 6, American Society of Mechanical Engineers, 2019.
[8] L. Löber, F.P. Schimansky, U. Kühn, F. Pyczak, J. Eckert, Selective laser melting of a beta-solidifying TNM-B1 titanium aluminide alloy, J. Mater. Process. Technol. 214 (2014) 1852–1860.
[9] S. Biamino, A. Penna, U. Ackelid, S. Sabbadini, O. Tassa, P. Fino, M. Pavese, et al., Electron beam melting of Ti–48Al–2Cr–2Nb alloy, Intermetallics 19 (2011) 776–781.
[10] V. Juechter, C. Körner, Creep properties of Ti-48Al-2Cr-2Nb produced by selective electron beam melting, Key Eng. Mater. 704 (2016) 190–196.
[11] V. Juechter, M.M. Franke, T. Merenda, A. Stich, C. Körner, R.F. Singer, Additive manufacturing of Ti-45Al-4Nb-C by selective electron beam melting for automotive applications, Addit. Manuf. 22 (2018) 118–126.
[12] M. Terner, S. Biamino, P. Epicoco, A. Penna, O. Hedin, S. Sabbadini, P. Fino, et al., Electron beam melting of high niobium containing TiAl alloy, Steel Res. Int. 83 (2012) 943–949.
[13] M. Todai, T. Nakano, T. Liu, H.Y. Yasuda, K. Hagihara, K. Cho, M. Ueda, et al., Effect of building direction on the microstructure and tensile properties of Ti-48Al-2Cr-2Nb alloy additively manufactured by electron beam melting, Addit. Manuf. 13 (2017) 61–70.
[14] R. Wartbichler, H. Clemens, S. Mayer, Electron beam melting of a β-solidifying intermetallic titanium aluminide alloy, Adv. Eng. Mater. 21 (2019) 1900800.
[15] G. Paulo, Titanium Aluminide - 4 Manufacturing Processes for 1 Blade, Mölndal, 2019.
[16] S.-.C. Huang, E.L. Hall, Plastic deformation and fracture of binary TiAl-base alloys, Metall. Trans. A 22 (1991) 427–439.
[17] S.-.C. Huang, E.L. Hall, The effects of Cr additions to binary TiAl-base alloys, Metall. Trans. A 22 (1991) 2619–2627.
[18] F. Appel, J.D.H. Paul, M. Oehring, Gamma Titanium Aluminide Alloys: Science and Technology, Wiley, Weinheim, 2012.
[19] S.-.C. Huang, Titanium aluminum alloys modified by chromium and niobium and method of preperation(4879092), 1989.
[20] H. Clemens, W. Wallgram, S. Kremmer, V. Güther, A. Otto, A. Bartels, Design of novel β-solidifying TiAl alloys with adjustable β/B2-phase fraction and excellent hot-workability, Adv. Eng. Mater. 10 (2008) 707–713.

[21] U. Habel, F. Heutling, D. Helm, C. Kunze, W. Smarsly, G. Das, H. Clemens, Forged intermetallic γ-TiAl based alloy low pressure turbine blade in the geared turbofan, in: Proceedings of the 13th World Confrence on Titanium, 2016.
[22] E. Schwaighofer, H. Clemens, S. Mayer, J. Lindemann, J. Klose, W. Smarsly, V. Güther, Microstructural design and mechanical properties of a cast and heat-treated intermetallic multi-phase γ-TiAl based alloy, Intermetallics 44 (2014) 128–140.
[23] S.S. Al-Bermani, M.L. Blackmore, W. Zhang, I. Todd, The origin of microstructural diversity, texture, and mechanical properties in electron beam melted Ti-6Al-4V, Metallur. Mater. Trans. A 41 (2010) 3422–3434.
[24] M. Schloffer, Method for producing a component from a graded TiAl alloy and component produced therefrom(US 2019/0299288 A1), 2019.
[25] W. Smarsly, M. Schloffer, H. Clemens, T. Klein, High temperature resistant TiAl alloy, production method therefor and component made therefrom(US 2018/0016668 A1), 2017.
[26] W. Smarsly, M. Schloffer, H. Clemens, S. Mayer, Al-reiche Hochtemperatur-TiAl-Legierung(EP3 054 023 B1), 2014.
[27] L.E. Murr, S.M. Gaytan, A. Ceylan, E. Martinez, J.L. Martinez, D.H. Hernandez, B.I. Machado, et al., Characterization of titanium aluminide alloy components fabricated by additive manufacturing using electron beam melting, Acta Mater. 58 (2010) 1887–1894.
[28] Dr.P. Calza, Additive Manufacturing @ Avio Aero, Mölndal, 2019.
[29] C. Körner, Additive manufacturing of metallic components by selective electron beam melting — A review, Int. Mater. Rev. 61 (2016) 361–377.
[30] A. Bauereiß, T. Scharowsky, C. Körner, Defect generation and propagation mechanism during additive manufacturing by selective beam melting, J. Mater. Process. Technol. 214 (2014) 2522–2528.
[31] A.M. Rausch, M. Markl, C. Körner, Predictive simulation of process windows for powder bed fusion additive manufacturing, Comput. Math. Appl. 78 (2019) 2351–2359.
[32] M. Bayat, A. Thanki, S. Mohanty, A. Witvrouw, S. Yang, J. Thorborg, N.S. Tiedje, et al., Keyhole-induced porosities in Laser-based Powder Bed Fusion (L-PBF) of Ti6Al4V, Addit. Manuf. 30 (2019) 100835.
[33] J. Bruno, A. Rochman, G. Cassar, Effect of build orientation of electron beam melting on microstructure and mechanical properties of Ti-6Al-4V, J. Mater. Eng. Perform. 26 (2017) 692–703.
[34] Y.-W. Kim, Effects of microstructure on the deformation and fracture of γ-TiAl alloys, Mater. Sci. Eng.: A 192-193 (1995) 519–533.
[35] T. Leitner, M. Schloffer, S. Mayer, J. Eßlinger, H. Clemens, R. Pippan, Fracture and R-curve behavior of an intermetallic β-stabilized TiAl alloy with different nearly lamellar microstructures, Intermetallics 53 (2014) 1–9.
[36] V. Jüchter, Grundlagen des Selektiven Elektronenstrahlschmelzens von Titanaluminiden, 2019.
[37] H.F. Chladil, H. Clemens, A. Otto, V. Güther, S. Kremmer, A. Bartels, R. Gerling, Charakterisierung einer β-erstarrenden γ-TiAl-Basislegierung, BHM Berg- und Hüttenmännische Monatshefte 151 (2006) 356–361.
[38] G. Baudana, S. Biamino, B. Klöden, A. Kirchner, T. Weißgärber, B. Kieback, M. Pavese, et al., Electron beam melting of Ti-48Al-2Nb-0.7Cr-0.3Si, Intermetallics 73 (2016) 43–49.
[39] A. Klassen, V.E. Forster, V. Juechter, C. Körner, Numerical simulation of multi-component evaporation during selective electron beam melting of TiAl, J. Mater. Process. Technol. 247 (2017) 280–288.
[40] Deutsches Institut für Normung, Metallische Werkstoffe - Zugversuch: DIN EN ISO 6892 = Metallic materials - tensile testing = Matériaux métalliques - essai de traction, Beuth, Berlin, 2009.
[41] Deutsches Institut für Normung, DIN EN ISO 204, Beuth Verlag GmbH, Berlin, 2019.
[42] S. Mayer, E. Schwaighofer, M. Schloffer, H. Clemens, The use of *In Situ* characterization techniques for the development of intermetallic titanium aluminides, Mater. Sci. Forum 783-786 (2014) 2097–2102.
[43] G. Dehm, C. Motz, C. Scheu, H. Clemens, P.H. Mayrhofer, C. Mitterer, Mechanical size-effects in miniaturized and bulk materials, Adv. Eng. Mater. 8 (2006) 1033–1045.
[44] M. Schloffer, Gefüge und Eigenschaften der intermetallischen TNM-Legierung, Montanuniversität Leoben, 2013.
[45] J. Malaplate, M. Thomas, P. Belaygue, M. Grange, A. Couret, Primary creep at 750°C in two cast and PM Ti48Al48Cr2Nb2 alloys, Acta Mater. 54 (2006) 601–611.